Seasonal icings reveal subsurface water drainage of a Greenland Ice Sheet outlet glacier

Rebecca McCerery[1], Joseph A. Graly[1], Christopher L. Hansen[2], Kate Winter[1], William P. Gilhooly III[3], Trinity L. Hamilton[2,4], Moses Jatta[3], Jeff R. Havig[2], Felipe Napoleoni[1,5], Alicia M. Rutledge[6], Matthew Terrell[3], Tanya M. Trott[7], Kayla Woodie[3], Bernd Kulessa[7], Sevi Modestou[1], Hannah Bahrani[1], Tori Kennedy[3], Alexandra Messerli[8], Kathy Licht[3]

*Corresponding author becky.mccerery@manchester.ac.uk

[1]School of Geography and Natural Sciences, Northumbria University, Newcastle Upon Tyne, NE1 8ST, United Kingdom

[2]Department of Plant and Microbial Biology, University of Minnesota, Saint Paul, MN 55108 USA

[3]Department of Earth & Environmental Sciences, Indiana University Indianapolis, Indianapolis, IN 46202 USA

[4]The BioTechnology Institute, University of Minnesota, Saint Paul, MN 55108 USA

[5]School of Geosciences, University of Edinburgh, Edinburgh, EH8 9XP, United Kingdom

[6]Department of Astronomy and Planetary Science, Northern Arizona University, Flagstaff, AZ 86011 USA

[7]School of Biosciences, Geography and Physics, Swansea University, Swansea, SA2 8PP, United Kingdom

[8]Asiaq Greenland Survey: Nuuk, GL

Abstract

In many glacial settings, winter outflows of proglacial water create stratified domed ice structures on glacial forefields. These structures, called naledi, provide an opportunity to characterise solute concentrations in hydrological systems during winter, which are poorly constrained compared with summer outflows dominated by supraglacial meltwater. To characterise the different hydrological systems feeding naledi and provide conceptual models of their formation, we sampled 12 overwinter naledi and 4 summer ice accumulations (accreted ice) from the forefield of Isunnguata Sermia, a western outlet glacier of the Greenland Ice Sheet, during four field campaigns. Major ions and stable water isotopes reveal complex geochemical signatures, where the composition of successive naled layers indicates fluctuations in water source and transport throughout winter. In comparison, summer accreted ice is sediment laden and shows uniform geochemistry throughout, suggesting freeze-on of water from a single source in quick, discrete events. These findings are supported by Electrical Resistivity Tomography (ERT) geophysical surveys showing shallow hydrological pathways (1 – 5 m below the surface) in the glacial foreland (surveyed 400 m from the glacier terminus). These results inform the first conceptual models of summer vs. wintertime subglacial water routing and naled formation in the proglacial zone of the Greenland Ice Sheet. We show that wintertime naledi form from a combination of top-down (unconfined) and bottom-up (confined) freezing processes incorporating subglacial discharge, overland flow and precipitation. In contrast, accreted ice forms from upwellings of high-velocity, highly pressurised water which freezes upon release. These seasonal changes drive different geochemical and solute outputs, which are critical for evaluating glacier meltwater contributions to proglacial groundwater systems and the impact of glacial discharge on downstream ecosystems.

1. Introduction

The Greenland Ice Sheet is a major exporter of biologically important elements to the world's oceans (Hawkings et al., 2016; Lawson et al., 2014; Wadham et al., 2016) and a hotspot for CO_2 drawdown through chemical weathering processes (Graly et al., 2017a; Pain et al., 2021). Most of our knowledge of chemical and biological fluxes from the Greenland Ice Sheet comes from analysis of the summer ablation season outflow, where channelised melt waters contact only a limited portion of the glacier bed (Bhatia et al., 2013; Hawkings et al., 2016; Jacob et al., 2014; Meire et al., 2016; Yde et al., 2014). However, during winter, outflow is typically fed by slower-flowing subglacial meltwater, which has often been subjected to greater contact time with the ice/bed interface (Chandler et al., 2013; Davison et al., 2019). As there are inherent challenges associated with field sampling subglacial water flow over winter, there is limited inclusion of winter water in geochemical modelling, inhibiting our understanding of year-round subglacial weathering processes and nutrient export from Greenland.

In many proglacial environments in the Arctic, domed ice structures called naledi (singular *naled* but also referred to as *aufeis* or *icings*) develop within glacier forefields in the winter months (Carey, 1973; Hodgkins et al., 2004; Mallinson et al., 2019; Morse and Wolfe, 2015; Sobota, 2016; Yoshikawa et al., 2007). These naledi typically consist of stratified layers of frozen subsurface and subglacial water discharged over winter (November - March). As such, they provide a potential source for characterising wintertime solute concentrations and insights into chemical weathering processes operating over low-flow hydrological conditions that are difficult to obtain by other means. Layers build up over winter to produce a domed, layered, ice structure, which can reach multi-metre heights, forming where outflows of water are expelled in discrete locations of the glacial foreland and quickly freeze due to low air temperatures (Harden et al., 1977; Kane, 1981).

68 The prevailing theoretical models of naled formation, established ~40 years ago,
69 suggest that naled grow in a top-down fashion because the cold winter atmosphere acts as a
70 heat sink, freezing unconfined waters that accumulate from above (Fig. 1a-c) (Schohl and
71 Ettema, 1986; Yde et al., 2012). However, more recent and direct observations of proglacial
72 naled in Svalbard by Stachnik et al. (2016) interpreted naled formation as a primarily bottom-
73 up process. This theory suggests new meltwaters confined below ice push up older, frozen
74 layers (Fig. 1d-f), and that liquid water conduits within naled ice provide insulated transport
75 pathways, protected from the cold surface (Fig. 1f). These contrasting models of formation
76 make it challenging to extrapolate general chemical and biological insights into different
77 hydrological systems.
78 In previous research, principally on Svalbard, the chemistry preserved in naled ice has
79 been successfully characterised by analysing ice cores collected in early spring (Stachnik et al.,
80 2016; Wadham et al., 2000; Yde et al., 2012). These studies found that the overwinter solute
81 flux captured in naled differs significantly from the early spring or late summer meltwater
82 output from glacial systems, suggesting they can capture a distinct wintertime hydrochemical
83 regime (Graly et al., 2018). However, complexity in their geochemistry indicates multiple
84 water source inputs may build up a single naled (Yde et al., 2012) with chemical differences
85 between different ice layers (Stachnik et al., 2016). The glaciers of Svalbard represent
86 relatively small glacier hydrologic systems, with small storage capacities compared to larger
87 ice sheets, like the Greenland Ice Sheet and its outlet glaciers (Wadham et al., 2000). It is
88 therefore possible that the chemical signatures of naled ice in these larger systems may
89 represent different formation mechanisms than those in Svalbard. In glacial foreland areas,
90 supercooled waters can also freeze and build up accreted ice structures over summer, often
91 during high discharge events sourced from glacial overdeepenings that are heavily sediment-

laden (Alley et al., 1998; Evenson et al., 1999; Lawson et al., 1998; Roberts et al., 2001; Roberts et al., 2002; Livingstone et al., 2026).

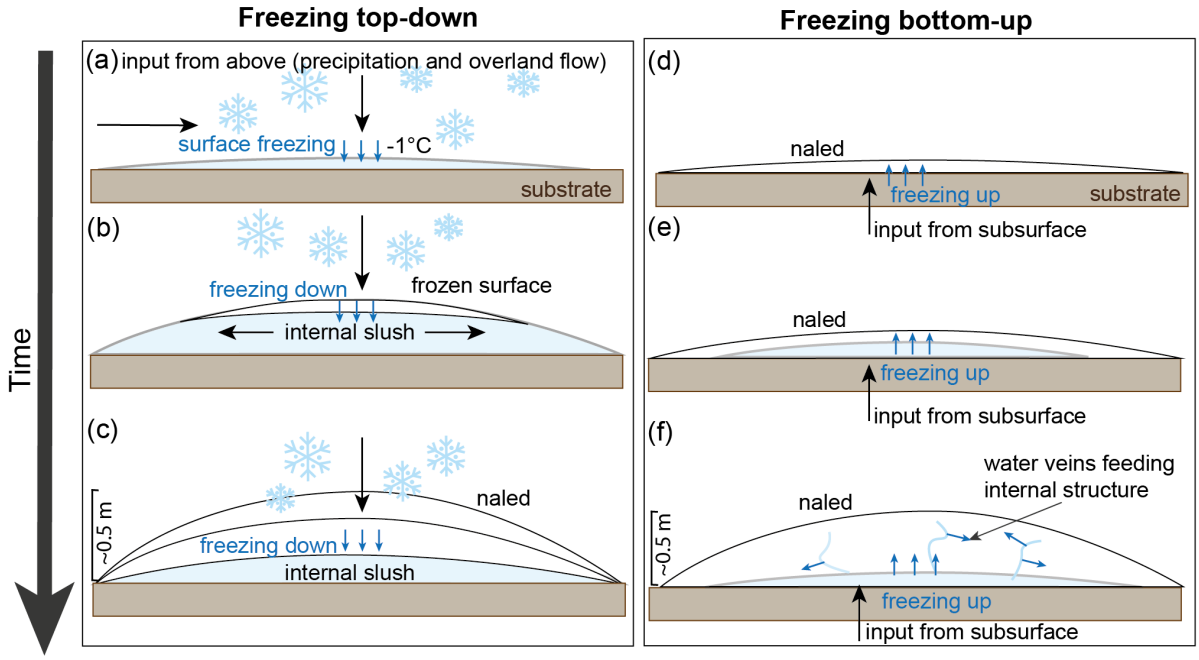


Figure 1 Prevailing theories of naled ice formation. (a-c) A top-down freezing process by which overland flow and precipitation freeze at the surface due to subzero air temperatures (Schohl and Ettema, 1986). (d-f) A bottom-up freezing process by which subsurface waters erupt into the forefield and freeze from the base-up, with newly erupting waters accreting onto the bottom of the naled. In these bottom-up models, there is also potential for small water veins within the naled to accrete ice within (Wadham et al., 2000; Stachnik et al., 2016).

Here, we measure and interpret the chemical characteristics and identify the sources of water creating wintertime naled ice and summertime accreted ice in the forefield of Isunnguata Sermia on the western Greenland Ice Sheet. We combine our geochemical analyses with geophysical surveys of the forefield to assess potential routing mechanisms of water flow feeding these structures and explore seasonal changes in the hydrological system. Our results inform a new conceptual model of naled and accreted ice formation applicable to similar proglacial systems in West Greenland and other glaciated regions.

2. Study site

Isunnguata Sermia (N67.1850, W-50.3394) drains ~15,900 km^2 of the Greenland Ice Sheet and is located approximately 100 km away from the coast (Fig. 2) (Lindbäck et al., 2015). The outlet glacier is located in the central west region of Greenland, routed through an overdeepened bed (extending to ~350 m below sea level) for over 20 km (Lindbäck et al., 2015). Throughout its catchment area, Isunnguata Sermia is expected to flow over granodioritic gneisses and associated silicate rocks of the Nassuttooqidian Orogen, a large-scale fold-belt formed c. 2.7 billion years ago (van Gool et al., 2002).

Previous work has characterised spring/summer runoff and subglacial hydrology at Isunnguata Sermia (Bartholomew et al., 2011; Meierbachtol et al., 2013) as well as subglacial discharge and hydrochemistry of summer outflows (Graly et al., 2017a). Wintertime outflow was chemically profiled by Pitcher et al. (2020), who sampled proglacial river water while performing local radar surveys of Isunnguata Sermia. This revealed that basal water is persistent at Isunnguata Sermia, discharging small amounts of water into the proglacial river system year-round. Isunnguata Sermia also sits on a reverse gradient bed slope with an active subglacial lake system (Livingstone et al., 2019). These lakes, located beneath the ablation zone of Isunnguata Sermia, have been shown to exhibit multi-year water storage, resulting in long water residence times, though research has also shown that meltwater can be quickly released during flood events (Chu et al., 2016; Livingstone et al., 2019).

The forefield of Isunnguata Sermia contains several discrete upwellings of subglacial water. These waters may emerge slowly, or as geyser-like features that expel water into the air on a metre- to multi-metre scale (Livingstone et al., 2026). In February 2015, supercooled water was discovered below the clear ice of a proglacial outlet stream, 1 km downstream of the Isunnguata Sermia terminus (Pitcher et al., 2020). This slow meltwater drainage, fed by the deeply incised subglacial trough that extends inland from the terminus (Graly et al., 2017a),

suggests that the local geometry might drive proglacial upwellings of subglacial meltwater year-round. As a result, this site provides an ideal location to investigate the geochemical signature of water sources feeding naled ice and accreted ice, allowing us to examine changes in hydrological pathways and fully characterise the chemical signature of year-round outflows, for the first time.

3. Methods

3.1. Automatic cameras

Monitoring of glacier outflow and the development of naledi was done by setting up time-lapse cameras (LTL-6210MC Plus Scouting Cameras) across the glacier forefield and monitored between 2022 and 2024 (Fig. 2 and Table SI1). Cameras were set up at six different locations and orientations to capture changes in the main outflow channel of Isunnguata Sermia and to review active upwellings at the time of installation. Photographs were taken at 11 am, 12 pm, 1 pm and 2 pm (local time) each day. Full descriptions of camera installations and observations can be found in Supplementary Information Table SI1.

3.2. Sampling

Four field campaigns were conducted to collect a representative sample set of ice and water samples across the Isunnguata Sermia forefield over multiple years both pre- and post-melt season (Fig. 2). We focused on three different sample types (i) naled ice (dome shaped structures, formed over winter likely during low discharge), (ii) naled waters upwelling in the outwash plain (capturing active water sources feeding naled ice over the winter months) and (iii) accreted ice (sediment-laden ice structures associated with active upwellings in the summer months) (Fig. 2).

Over the course of four field campaigns (October 2022, April 2023, September 2023 and March-April 2024), we sampled 12 naledi and 4 accreted ice structures (Fig 2a, Fig. S1-

158 2). Ice cores were extracted with a motorised SIPRE Auger to a maximum depth of 2 m. Cores
159 were logged immediately, then sectioned by changes in ice facies and transported in individual
160 sterile Whirl-Pak bags (Fig. 3). Core sections were then melted in a gently heated water bath
161 in the field (less than 4 hours after sampling) and filtered using Whatman 0.45μm cellulose
162 membrane filters into centrifuge tubes for major ion analysis. All samples were refrigerated
163 and stored at 3-4°C until analysis. Four of the naled ice cores terminated in water sources.
164 Cores at the other seven sites did not reach water and were limited to depths between 8 and
165 139 cm, often due to thick gravel deposits which rendered further drilling impossible.
166 Of the cores that reached active water sources, naled I8 was located at the margin of
167 the main meltwater channel and the three others (I2, I3 and I10) in an adjacent lateral meltwater
168 stream (Fig. 2). In each case, samples of the naled upwelling waters were collected in sterile
169 50 mL centrifuge tubes and filtered using Whatman 0.45 μm nylon membrane filters. Accreted
170 ice cores were sampled around the glacier front and within the main active frozen meltwater
171 channel area in October 2022 (n = 4, Fig. 2a, Fig. 4 and Fig. S3). Unlike the naled ice core
172 sites, none of the accreted ice cores reached free-flowing waters.

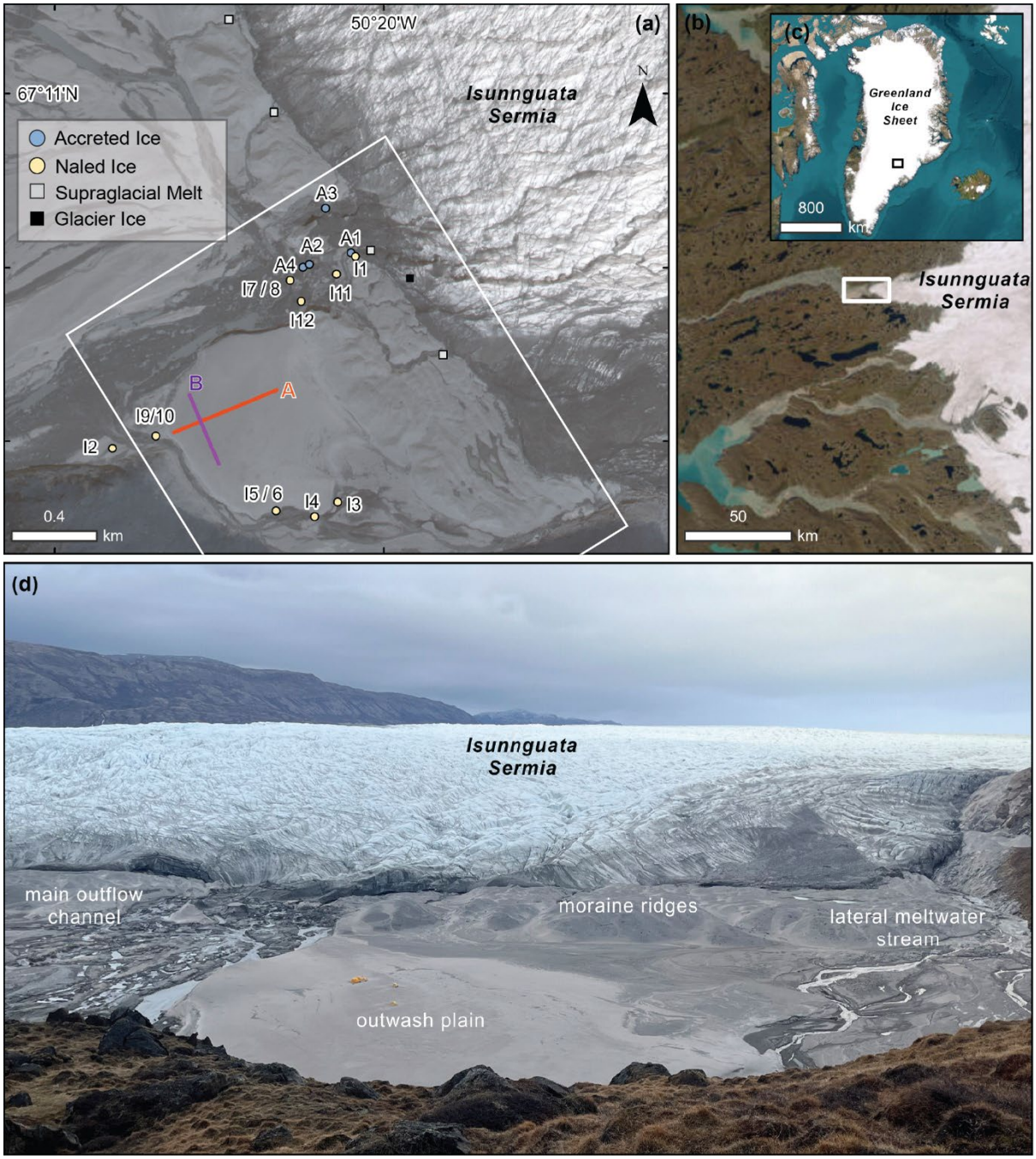


Figure 2. Isunnguata Sermia field site in West Greenland (a) Location of sampling sites, geophysical survey transects (A and B) and camera trap locations in the forefield of Isunnguata Sermia. White box denotes the photograph area shown in (d). (b) Sample area of the Isunnguata Sermia forefield (white box), where meltwater is exported from the Greenland Ice Sheet (c). (d) Overview photograph of the proglacial forefield from May 2023 with key sites annotated. The yellow features on the outwash plain are camp tents, approximately 1.6-1.9 m high. Imagery © [2024] Vantor in panel (a) sourced from the Polar Geospatial Centre (showing June 2022) whilst panels b-c show Esri basemap imagery | Powered by Esri.

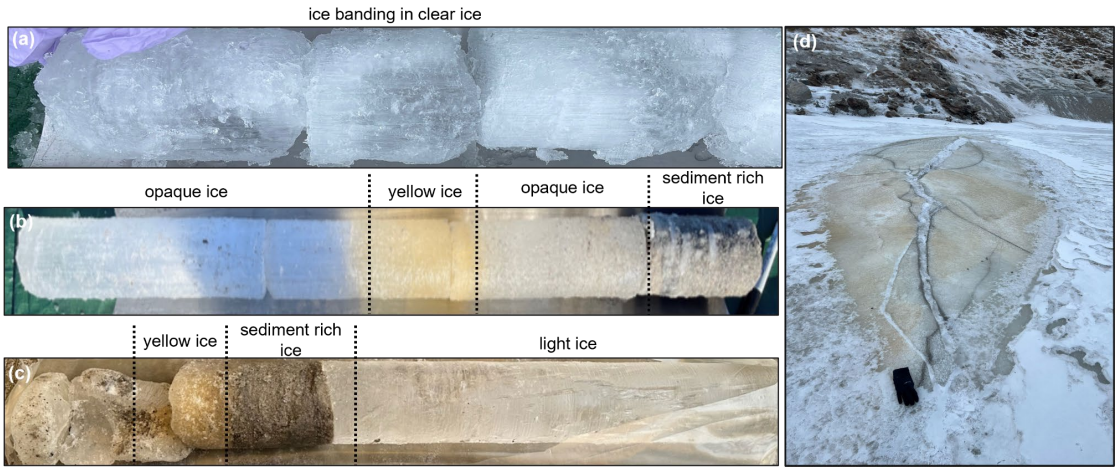


Figure 3 Naled ice structures and examples of different ice facies from cores. (a) Core I3 (15 cm), (b) upper 90 cm of core I10 and (c) lower 68 cm of core I10, as well as a photograph of a naled structure (cored for I10) (d) where a black glove (~20 cm in length) is provided for scale.

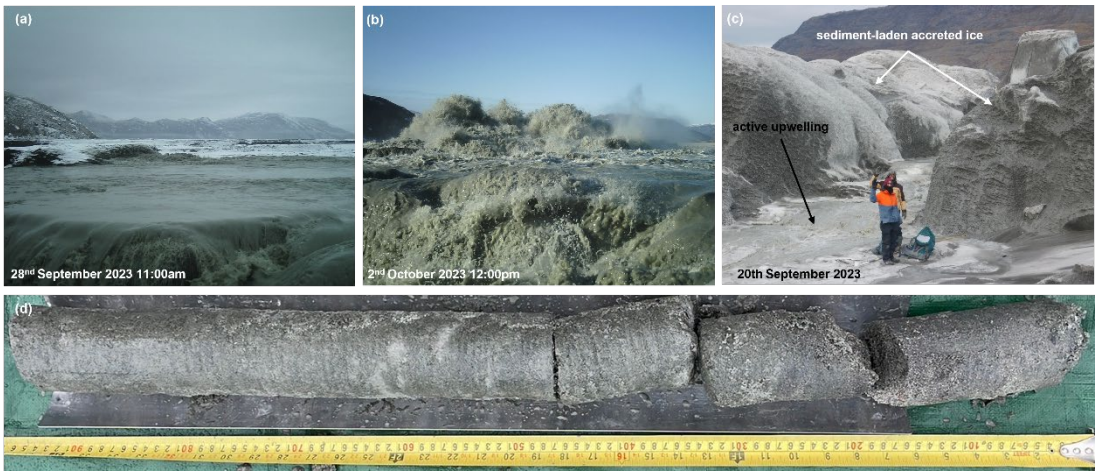


Figure 4 (a-b) Examples of a subglacial water outburst from Isunnguata Sermia, captured by automatic camera 4 in late September to early October 2023. Photographs show high water flow volumes on the 28th of September (a) followed by an erupting outflow 4 days later (b). (c) Example of a multi-metre high accreted ice structure, alongside an active, bubbling upwelling of water, reviewed by field researchers on the 20th of September 2023. (d) Example of a sediment-rich core from an accreted ice structure.

Contextual samples of glacier ice (n = 2) and supraglacial meltwater (n = 7) were also collected to represent end-member water types. Glacier ice was sampled from the upper ice margin of Isunnguata Sermia in April 2024 using a chisel and hammer, with the upper 10 cm layer of ice discarded to remove the outer layer of weathered ice (Fig. 2a). Supraglacial water was sampled from the ice margin and atop the Isunnguata Sermia glacier snout in 50 mL centrifuge tubes.

3.3. Geochemistry

Concentrations of major anions in water and melted ice samples were analysed in triplicate on a Dionex Integrion high-pressure ion chromatography (IC) system at Northumbria University using 5 mL of sample. Standard solutions of fluoride (F^-), chloride (Cl^-), sulphate (SO_4^{2-}), and nitrate (NO_3^-) were prepared using 18.2 MΩ ultrapure water to obtain standard curves. Concentrations of major cations were analysed in triplicate on an Optima 8000 inductively coupled plasma optical emission spectrometer (ICP-OES) at Northumbria University using 7 mL of sample. Standard solutions of calcium (Ca), potassium (K), magnesium (Mg), and sodium (Na) were prepared using ultrapure water to obtain standard curves. Limits of detection (LOD) for both instruments was determined by standard regression on the intercept of the calibration curve and measured 0.02 mg L^{-1}. Analytical precision was assessed as the relative standard deviation (RSD %) of triplicate measurements for each sample. RSD was below 3% for all analytes and across all run days for the ICP-OES and the IC, indicating good analytical reproducibility. HCO_3^- was then calculated using the charge balance error (CBE) method, where ε^+ and ε^- are total cation and anion equivalents. Uncertainty in HCO_3^- concentrations is derived from uncertainties of all measured cation and anion concentrations.

3.4. Stable water isotopes

Aliquots of samples were analysed for their hydrogen and oxygen isotopic composition using a Picarro L2130-i cavity ringdown spectrometer at Northumbria University. Four calibration standards were measured at the beginning of each run (including in-house laboratory standards supplied and calibrated by the University of Bergen ('EVAP-2', 'FINSE', 'GLW') and international standard SLAP2 (Standard Light Antarctic Precipitation 2). Separate aliquots of reference water 'Medium Natural Water ' or 'Greenland Water' (purchased from Elemental Microanalysis Ltd.) were analysed every 10 to 15 samples to monitor and correct instrument drift. Results were corrected for memory and drift and normalised to the VSMOW-SLAP (Vienna Standard Mean Ocean Water – Standard Light Antarctic Precipitation) scale, using the FARLAB Liquid Water Isotope Measurement Processor (FLIIMP) software package (Sodemann et al., 2023). No humidity correction was applied (following Weng et al., 2020). The drift standards (as well as one aliquot of VSMOW2 per run) were used as data quality monitors. Analytical error is equal to or better than 0.4‰ for δD and 0.07‰ for $\delta^{18}O$ (SE); overall reproducibility based on monitor standards is equal to or better than 1.0‰ for δD, and 0.38‰ for $\delta^{18}O$ (SD) (Table SI2). Individual 'freezing packages', which are discrete isotopic units within the naled ice body representing a temporally distinct episode of water upwelling and subsequent freezing at the ice surface, were also identified by calculating freezing curves for each ice core. In the context of refreezing Greenland Ice Sheet waters, a $\delta D:\delta^{18}O$ slope of around 6 would be expected. The composition of the source water can be calculated from the two-isotope slope (Souchez and Jouzel, 1984), allowing us to determine the isotopic composition of the source water where a freezing slope is identified.

3.5. Electrical Resistivity Tomography

A SuperSting R8 eight-channel earth resistivity metre (Advanced Geosciences, Inc.) was used to investigate subsurface conditions and potential water transport routes through the forefield

of Isunnguata Sermia (Fig. 2) in April 2024. The frozen ground had to be prepared for electrode stake deployment by thawing small areas to a depth of ~30 cm using boiled water, heated from locally sourced snowmelt. A mixture of locally sourced glacial clay and salt or isotonic powder (Gatorade^{TM}) was poured over the thawed ground to secure each electrode stake and ensure sufficient ground coupling once the electrodes froze in. Fifty-six electrodes were installed in a forward and reverse dipole-dipole configuration along profile A with the same configuration along profile B (Fig. 2) for 47 electrodes. The maximum source current was set to 50 mA for both profiles, and electrode contact resistance was monitored throughout. All data were processed and inverted using ResIPy v3.6.3 (Blanchy et al., 2020) (see Supplementary Information).

4. Results

4.1. Automatic cameras and Field Photos

Automatic cameras captured active naled and accreted ice formation as well as changes in winter outflow over the foreland of Isunnguata Sermia from 2022 to 2024. In 2023, Camera 5, orientated on the proglacial outwash plain facing the ice margin, captured the formation of winter-accumulating naled ice and an outflow of yellow-coloured water on the 22nd of October when the rest of the meltwater channel was frozen (Fig. 5). The source of flow from this yellow water originate from a location off-camera. The distinct colouration of this water can be seen freezing over the channel and naled structure over 3 days, before being covered by fresh snow on 28th October. These accumulation patterns suggest that similar ice layering may be expected in the naled icings.

A glacial outburst flood from Isunnguata Sermia was also detected between September and early October 2023 (see Livingstone et al. 2026). By analysing footage from two separate automatic cameras and orientations (see Supplementary Information), a gradual increase in

265 water levels of the main meltwater channel was observed before a vigorous outburst flood
266 event on October 2nd (Fig. 4a-b). We also observed the sudden build-up of sediment-laden
267 accreted ice around the upwelling during the outburst event (Fig. 6). Much of the resulting
268 accreted ice structure persisted up to 6 months later, preserved by the cold winter temperatures,
269 though it appeared to have eroded, suggesting some melt wastage had occurred.
270
271

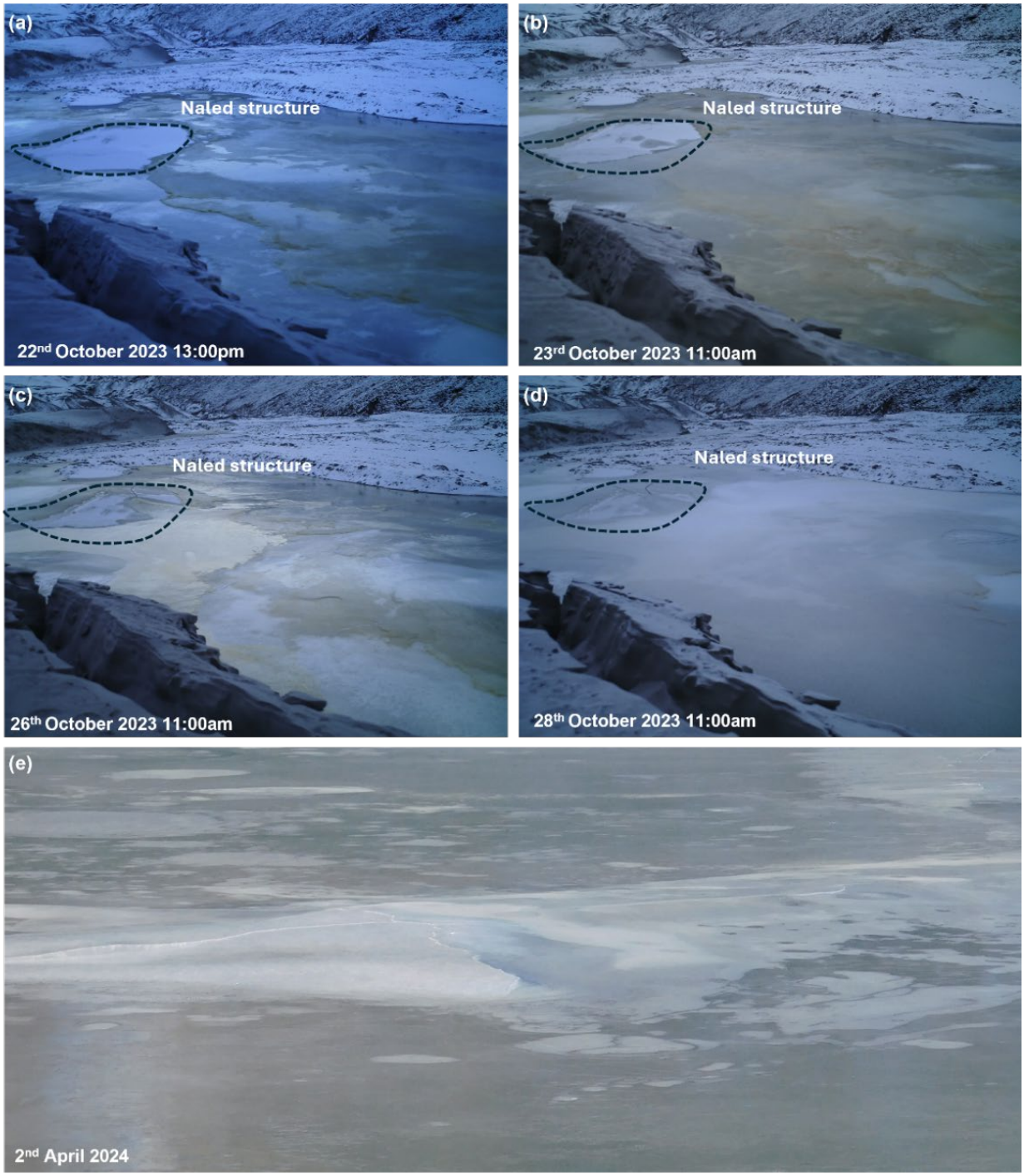


Figure 5 Upwelling of glacial waters in the forefield of Isunnguata Sermia, captured by an automatic camera installation (Camera 5) for the 2023/2024 winter season (a-d). Over the course of 6 days, distinctly yellow-coloured water flows and ice accumulations were recorded, suggesting variable water/snow inputs/throughputs. (a) Photograph showing the first emergence of yellow-coloured water in the glacial foreland. (b) The yellow outflow completely covers the proglacial river in the field of view. (c) White ice and snow begin to overlay the yellow layer, which has frozen. (d) The yellow ice layer is fully covered with fresh white ice and snow. Black dashed outline highlights the naled ice area. (e) A naled dome formed in the centre of the proglacial stream overnight on the 2nd April 2024, captured in field photographs.



Figure 6 Accreted ice formation (a-d) captured by an automatic camera installation for the 2023/2024 winter season. (a-b) Over the course of a week an eruption of glacial meltwater occurred in the main proglacial meltwater channel close to the Isunnguata Sermia ice margin (Livingstone et al., 2026), see https://vimeo.com/manage/videos/1103612163. (c) This resulted in the rapid accumulation of ice accretions around the upwelling. (d) Over 6 months later, some ice persists around the upwelling source, preserved by the cold winter temperatures, though the ice structure appears deflated and eroded. A similar process is seen in (e), where sediment-rich ice accumulations around an upwelling site in late September 2023 had deflated and eroded substantially (f) the following April 2024.

4.2. Ice facies analysis

Ice cores revealed distinct ice facies, which we group into four classifications: light ice, opaque ice, yellow-coloured ice, and sediment-rich ice (Fig. 3). Some ice has either horizontal or vertical stripes – which are more visible in the 'light ice' and 'opaque ice'. Light ice and opaque ice packages do not have sediment inclusions or discolouration, with the light ice mostly translucent and the opaque white or 'clouded ', and were combined for geochemical analysis as 'clear ice' for simplicity. Yellow-coloured ice was distinctly yellow in colour and appeared as discrete layers within the naled cores. Five ice cores recorded these yellow-coloured ice layers, which ranged in thickness from 10-25 cm, at various depths (Fig. 7b, e; Fig. 8a, c, e). Yellow-coloured ice was not found in any of the accreted ice cores. Sediment-rich ice had clear sediment inclusions that accounted for >50% of the core section. Sediment layers were present in nearly all core samples (except I2, I7 and I8), with more pronounced sediment-rich layers (between 10-40 cm thick) recorded in I1, I3, I5 and I10 (Fig. 7 and 8). These sediment-rich layers only appeared as discrete layers within the naled cores, but they account for almost the full core length in the accreted ice cores (Fig. 3 and 4). Facies logs for each ice core and their resultant geochemical profiles are provided in Figures 7, 8 and 9.

Accreted ice cores were typically multi-metre in length and consisted of heavily sediment-laden ice (Fig. 4), which appeared to be a mix of frazil ice and silt to fine sand sediments. Cores ranged in length from ~25 to 240 cm (Fig. 9). The longest core, A4, had no visible layers, but the full core was sediment-laden with clay to fine sand-sized particles (Fig. 4d). Bands of opaque ice, less than 10 cm thick, were recorded at various intervals throughout cores A1, A2 and A3.

4.3. Geochemistry

Proportions of major ions and total dissolved solids (TDS) are shown for each core in Fig. 7, 8 and 9. The naled ice cores and their sub-naled waters display a range of TDS concentrations,

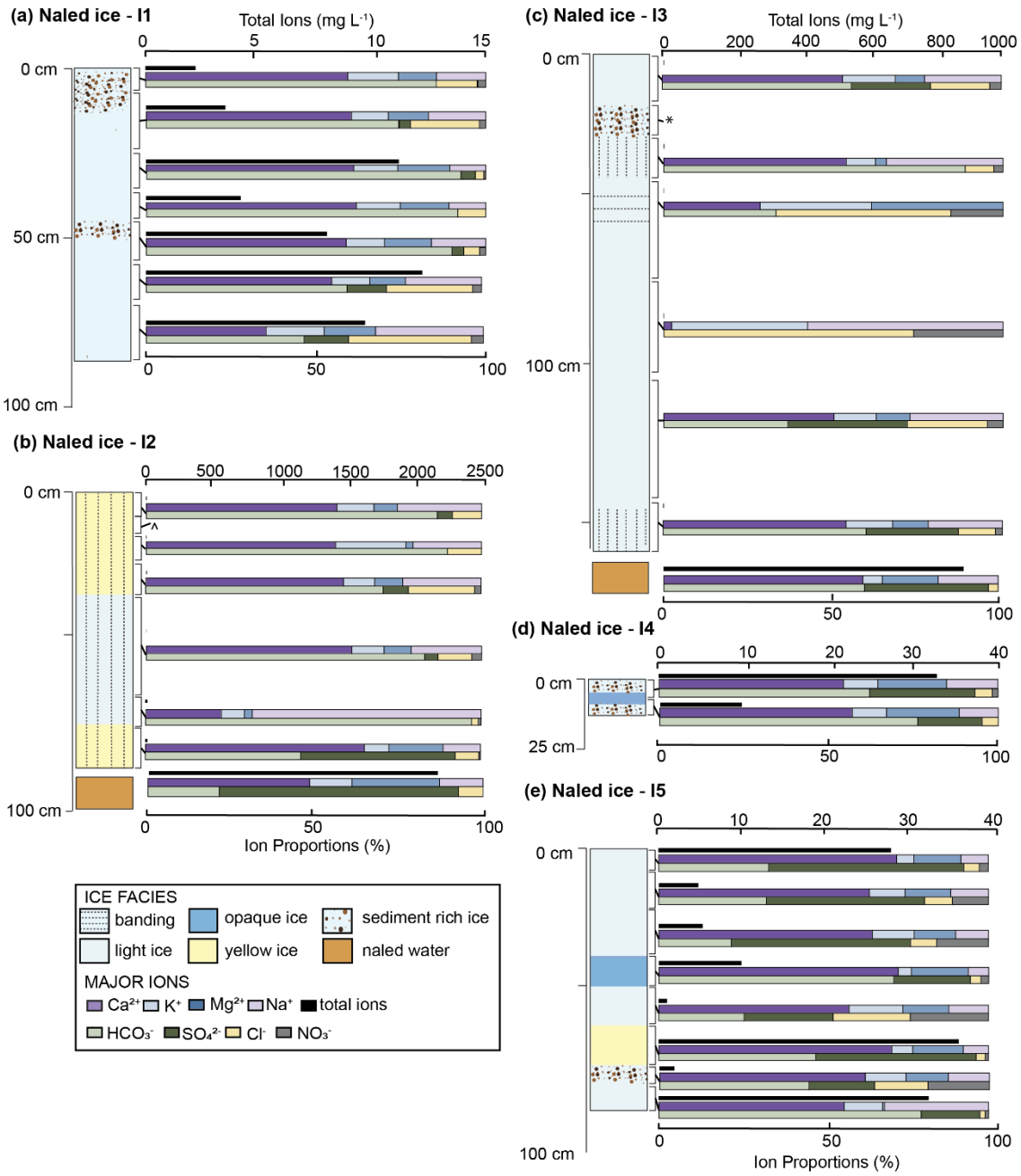
broadly spanning from very dilute (less than 1 mg L^{-1}) to highly concentrated (up to 3,000 mg L^{-1}) depending on the core and depth. Across most cores, HCO_3^- is the dominant anion, while Ca^{2+} is consistently the most abundant cation. In general, we observe that ice layers with low TDS, such as naled I1 and lower I7 (Fig. 7a, Fig. 8b), are typically SO_4^{2-} poor (though sometimes NO_3^- enriched). Whereas very concentrated TDS such as the naled waters in I2 and I3 (Fig.7b and c) are more often SO_4^{2-} enriched and have higher TDS concentrations than the overlying ice.

Naled cores I1, I7, I8, I11 and I12 were all located in the main proglacial river channel. Naled I1 was located closest to the glacier and extracted from beneath a layer of mud, whereas all other naled icings were collected from clean ice surfaces. All cores sampled from the main channel lack yellow ice layers apart from I8, which had a distinct yellow layer at the very surface and yellow water at the base of the core (Fig. 8). These main channel cores generally exhibit moderate TDS concentrations, except I8, which reaches up to 132 mg L^{-1} at its base and 3,098 mg L^{-1} in the water. HCO_3^- dominance is consistent across all main channel cores, SO_4^{2-} contributions are relatively low compared to some side channel cores. NO_3^- is slightly more elevated in I8 than in the other main channel cores. I12 was sampled as a newly emerging naled with only a thin layer of domed ice extracted after it began forming in the main channel overnight in March 2024. Here, the very surface of the naled ice was sampled and showed moderate TDS concentrations of 24-40 mg L^{-1} with an almost even proportion of HCO_3^- and SO_4^{2-}.

Side channel cores, I2, I3, I4, I5, I6, I9 and I10 show greater variability in both TDS concentrations (2-500 mg L^{-1} in ice and 2,100 mg L^{-1} in naled waters) and ion proportions. While HCO_3^- and Ca^{2+} dominate, SO_4^{2-} contributes more proportionally across several cores, most notably the naled water in I2, I6, and I10. Core I10 is particularly distinct, with SO_4^{2-} comprising over 40% of total ions throughout and TDS values reaching up to 548 mg L^{-1} in

342 the yellow ice layers. Naled waters sampled beneath I2 and I3 also show higher TDS
343 concentrations of 2,030 mg L^{-1} and 1,032 mg L^{-1}, respectively.

344 Accreted ice cores (A1-A4) are more uniform in their geochemical signature both
345 within single cores and across cores (Fig. 9c-f). All cores have TDS concentrations between
346 13 and 39 mg L^{-1} (Fig. 9c-f). HCO_3^- and Ca^{2+} consistently dominate, comprising 50-80% of
347 anion and cation proportions, respectively. The most variability is seen in accreted core A4,
348 where SO_4^- dominates the anions in some of the core sections. Accreted cores also have
349 marginally higher proportions of K^+ compared to the naled ice cores.



350

351 **Figure** 7 Ice facies and geochemical profiles of major ions for naled ice cores I1 through
352 I5 collected April 2023 and March-April 2024. Vertical columns indicate ice facies types.
353 Geochemical results are illustrated with cumulative horizontal bars adjacent to sampling
354 depth (exact depth range indicated by black brackets). Total dissolved solids (TDS) are
355 given in mg L^{-1} (upper, black bar); note unique axis values for each core. For some
356 samples, values are so low that they plot as a point. The proportions of cations (middle
357 bar plot, Ca^{2+}, K^{+}, Mg^{2+}, and Na^{+}) and anions (lower bar plot, Cl^{-}, SO_4^{2-}, NO_3^{-}, and HCO_3^{-}
358) are given in percentages.

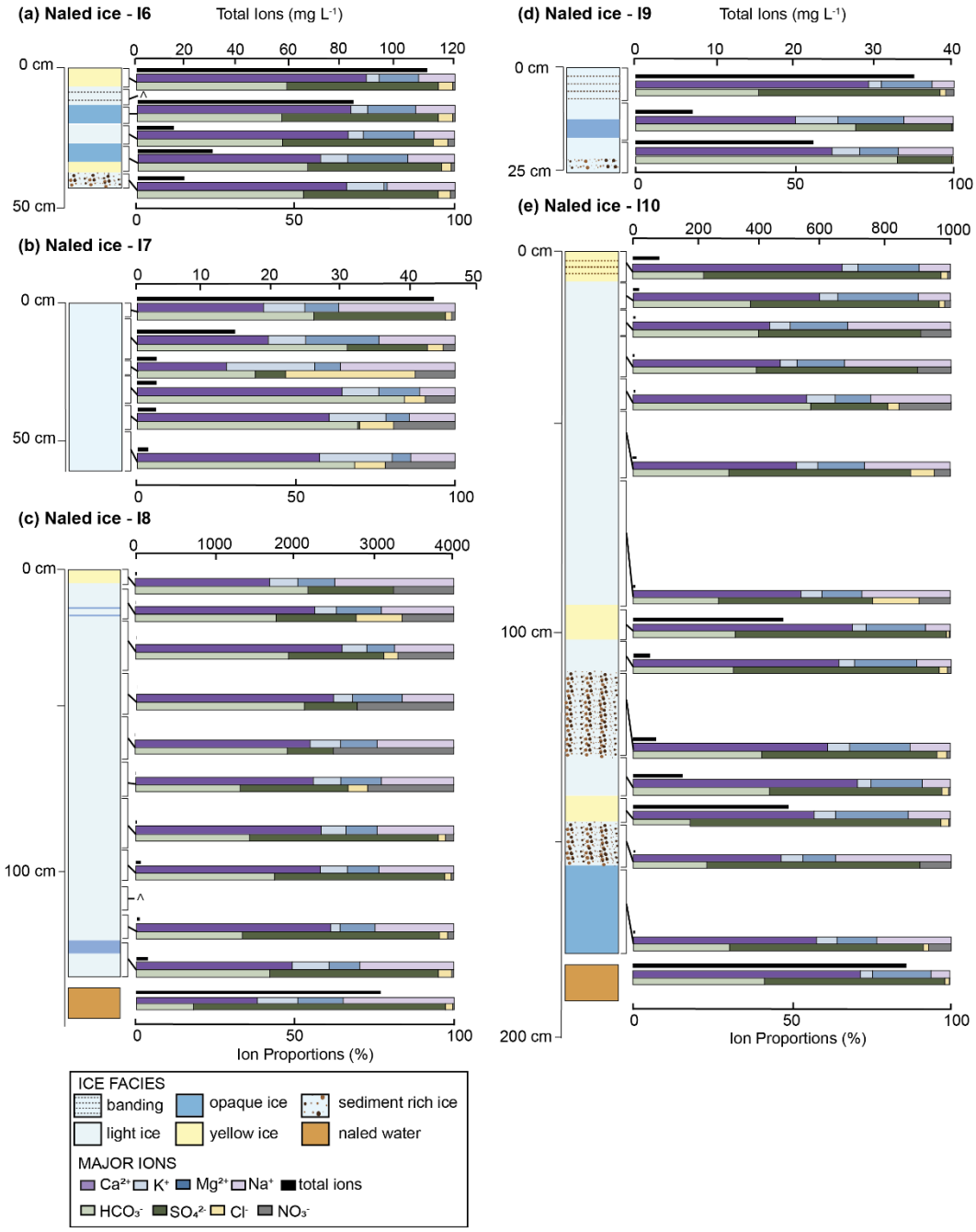


Figure 8 Ice facies and geochemical profile of major ions for naled ice cores I6 through I10 collected March-April 2024. Vertical columns indicate ice facies types and changes with depth. Geochemical results are illustrated with cumulative horizontal bars adjacent to sampling depth (exact depth range indicated by black brackets). TDS is given in mg L^{-1} (upper bar; note unique charge range for each core) and the proportions of cations (middle bar plot, Ca^{2+}, K^{+}, Mg^{2+}, and Na^{+}) and anions (lower bar plot, Cl^{-}, SO_4^{2-}, NO^{3-}, and HCO_3^{-}) are given in percentages. ^Sample not analysed.

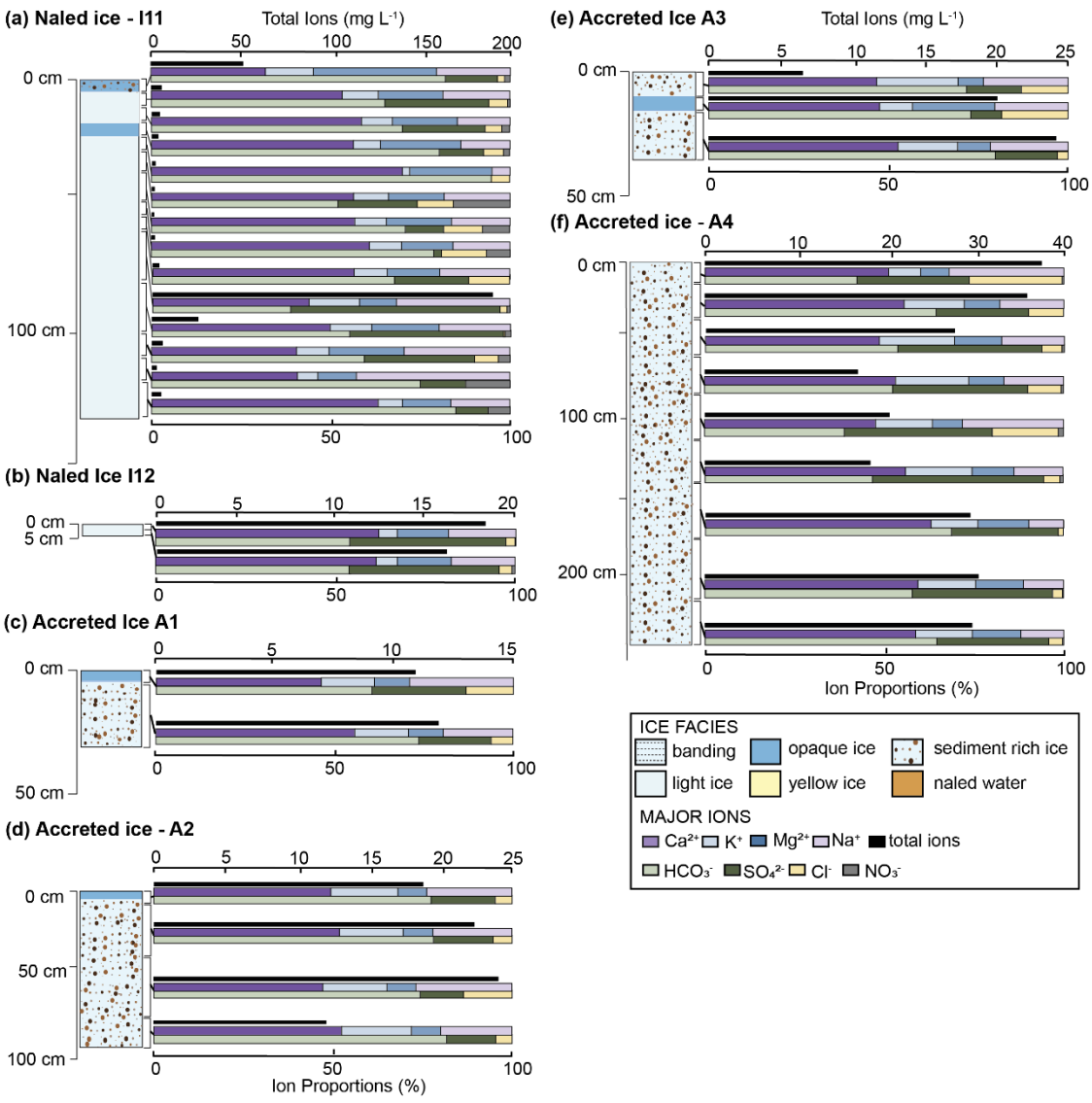
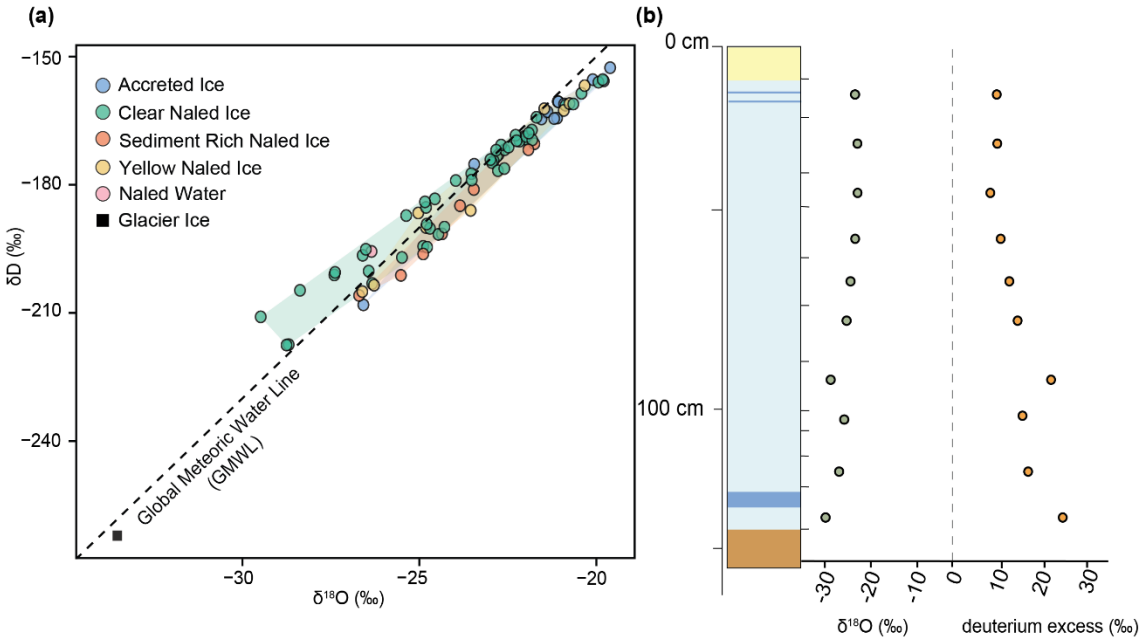


Figure 9 Ice facies and geochemical profile of major ions for naled ice cores I11 and I12 collected March-April 2024, and accreted ice cores collected October 2022 and April 2023. Vertical columns indicate ice facies types and changes with depth. Geochemical results are illustrated with cumulative horizontal bars adjacent to sampling depth (exact depth range indicated by black brackets). TDS is given in mg L^{-1} (upper bar; note unique charge range for each core) and the proportions of cations (middle bar plot, Ca^{2+}, K^{+}, Mg^{2+}, and Na^{+}) and anions (lower bar plot, Cl^{-}, SO_4^{2-}, NO_3^{-}, and HCO_3^{-}) are given in percentages.

4.4. Stable water isotopes

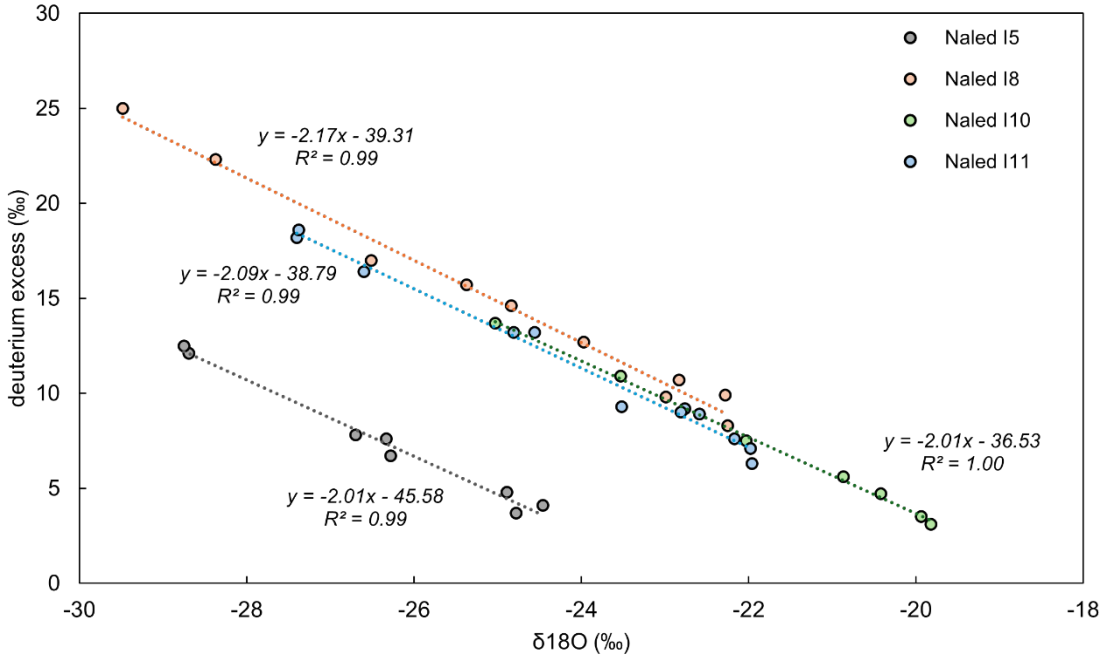
Isotopic compositions ($\delta^{18}O$ and δD) reveal accreted ice samples have slightly higher $\delta^{18}O$ and δD values (Fig. 10a; -21±1.7 ‰) compared to naled ice (Fig. 10a; -24±2.3 ‰). Surface glacier ice plots separately from all naled samples with the lowest $\delta^{18}O$ value (-33.5 ‰), indicating the naled ice is distinctly different in water source and/or formation mechanism than surface glacier ice (Fig. 10a). Deuterium excess ($D\text{-}excess = \delta^2H - 8 \cdot \delta^{18}O$) values range from approximately 3 ‰ to 32 ‰ with a general trend of decreasing deuterium excess with increasing $\delta^{18}O$ values (Fig. 11).

Changed in isotopic composition were also observed down-cores, revealing potential freezing mechanisms. Within naled core I8 (Fig. 10b) $\delta^{18}O$ values generally decrease downcore (the lowest values detected at 132-146 cm of -29.5 ‰) whereas deuterium excess increases from 9.8 ‰ at the top of the core to 25 ‰ at the base due to increasing fractionation processes downcore (Fig. 10b). However, a distinct but slight increase in $\delta^{18}O$ and decrease in deuterium excess was noted at 104-108 cm. When plotted on a freezing curve, naled ice samples I5, I8, I10 and I11 all display R^2 values of >0.9, suggesting sequential freezing downcore (Fig. 11). However, some core sections (in I2, I3, I4, I6, I7 and I9) do plot away from the freezing line with R^2 values of 0.07-0.93 (Fig. S4 in Supplementary Information). These sections represent discrete intervals of an increase in $\delta^{18}O$ and decrease in deuterium excess (also seen in Fig.10b), suggesting the start of a new freezing package.



396

397 **Figure 10** Summary of stable isotope analyses of different ice types. (a) Cross-plot of δD
398 vs $\delta^{18}O$ compared to the Global Meteoric Water Line (GMWL). (b) Down-core change
399 in $\delta^{18}O$ (green points) and deuterium excess (orange points) in naled core I8. Shaded
400 regions in a-c denote the range of isotope and chemical data for ice and water. Note, only
401 a subset of samples were analysed for stable water isotopes.



402

403 **Figure 11** Cross-plot of deuterium excess vs $\delta^{18}O$ of naled ice samples I5, I8, I10 and I11
404 on hypothesised freezing curves. All samples plot along the freezing curve with
405 increasing $\delta^{18}O$ and decreasing deuterium excess values with depth, indicative of
406 sequential freezing downcore.

4.5. Electrical Resistivity Tomography

Electrical Resistivity Tomography (ERT) surveys were conducted <400 m from the terminus of Isunnguata Sermia, in an area where gravel-rich sediments dominate (Fig. 2). The resulting ERT images (Fig. 12) reveal considerable spatial heterogeneity in subsurface resistivity, spanning from $\log_{10}\rho$ ~0.83 to >8.1. In both ERT profiles, the uppermost layer (~1 - 5 m below the surface) is dominated by high resistivity values ($\log_{10}\rho$ >10.5), often indicative of dry and (at least partially) frozen material (Kneisel et al., 2014). As the surface is dominated by unsaturated gravel-rich glacial outwash material and compacted till, we expect this uppermost subsurface layer is similar in character.

Beneath the high resistivity layer, an intermediate zone (approximately 5–15 m below ground level) exhibits markedly lower resistivities ($\log_{10}\rho$ ~2 - 4), varying across both profiles (yellow/white/blue colours in Fig. 12a). Bound by higher resistivity above and below, this zone likely represents a saturated sediment layer composed of sands/gravel and/or finer material or fractured bedrock (Palacky, 1987; Hauck & Kneisel, 2008; Reynolds 2011). Each of these materials can host groundwater, ice or subglacial meltwater. Localised zones of even lower resistivity ($\log_{10}\rho$ ~1- 2) are observed within this intermediate zone in both profiles (Fig. 12a, insets). Their geometry is suggestive of discrete pockets or conduits of moisture, potentially reflecting melting permafrost or glacial outflow pathways (e.g., Hauck & Kneisel, 2008). In both profiles, resistivity values abruptly return to $\log_{10}\rho$ ~10.5 and then $\log_{10}\rho$ ~10.6 Ωm beneath the intermediate zone. We interpret this to be drier sediments and/or frozen ground/ice (Kneisel et al., 2014), which would be likely in the forefield of Isunnguata Sermia in winter.

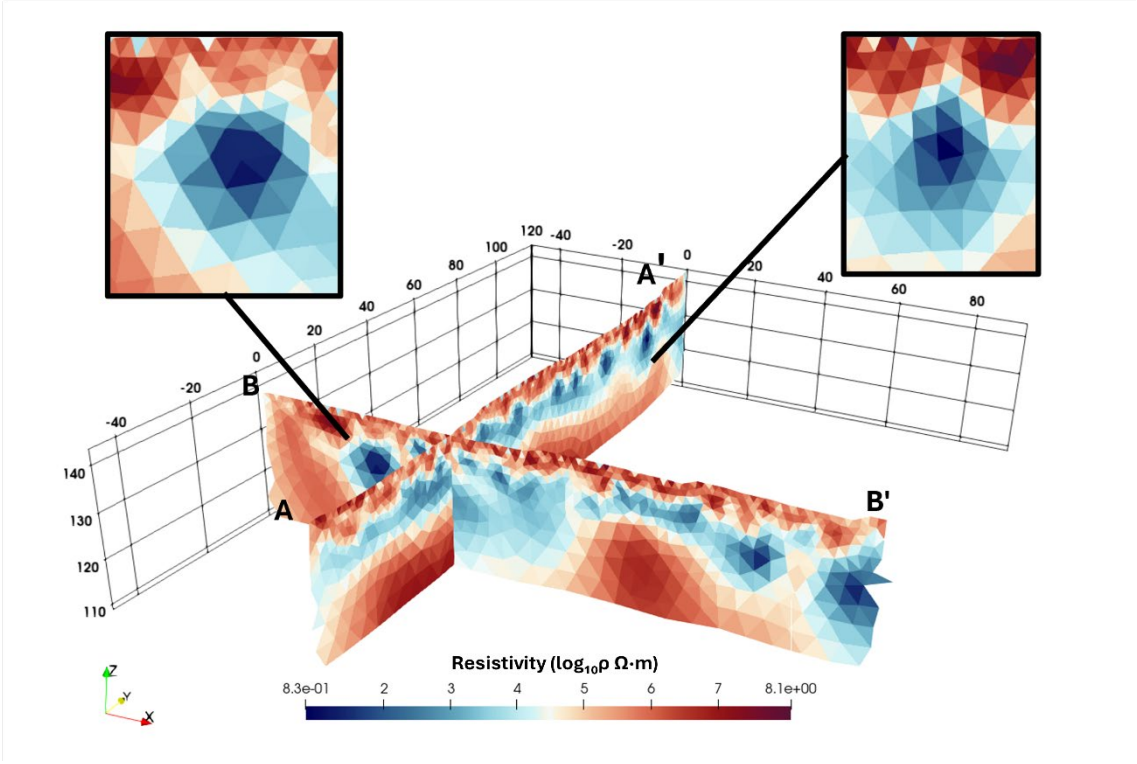


Figure 12 Two intersecting Electrical Resistivity Tomography (ERT) profiles surveyed in front of Isunnguata Sermia (location mapped on Figure 1). Depth and distance from starting location in metres. Resistivity values span a wide range (from $\log_{10}\rho$ ~1 to over 10.8), suggesting significant variations in moisture and/or porosity and/or liquid/frozen contrasts. Pockets of low resistivity, typical of high porosity or water-rich sediment zones, are shown in highlighted boxes.

5. Discussion

5.1. Naled ice formation mechanisms

Time-lapse camera footage, along with geochemical analyses of naledi and geophysical investigations of the glacial foreland at Isunnguata Sermia have allowed us to capture naledi formation mechanisms in unprecedented detail. Our data show icings forming under both confined and unconfined water input conditions.

In the confined condition, ice layers build up into dome-like structures, fed by the upwelling of waters from below (Fig. 5, 13). The waters likely originate from subglacial sources and are transported through subsurface conduits and/or saturated till (Fig. 12). In April 2024, naled ice domes were observed to have started forming overnight suggesting

447 that they may form quickly (Fig. 5e). Following formation of an ice layer that restricts
448 water flow, resultant build-up of water pressure beneath the naled can fracture the ice
449 surface (e.g. Fig. 5c). The method of formation we describe here is akin to the formation
450 mechanism described by Wadham et al. (2000) and Stachnik et al. (2016) (outlined in
451 Fig. 1d-f).

452 Not all of the naledi studied were exclusively fed from waters below, and our
453 results show that more than one formation mechanism exists with the incorporation of
454 unconfined waters from, for example, englacial flow or precipitation. Automatic camera
455 footage in Figure 5 demonstrates naledi being built from these unconfined waters, as ice
456 layers accumulate from overland water flow such as supra- and englacial melt and from
457 local precipitation such as the snow event captured in the automatic cameras (Fig. 13).
458 The cameras also captured the incorporation of yellow coloured waters originating off-
459 camera. Due to the colour similarity with the waters collected below naled structures, we
460 believe this overland flow originated from a large upwelling of overwinter waters at a
461 nearby naled location. These camera-derived observations, combined with geochemical
462 analysis, help to explain some of the unique ice facies we observed in the naled ice cores.

463 The waters with relatively high concentrations of TDS at the base of the naled cores
464 are interpreted to reflect prolonged water storage in the subglacial system (at least over
465 the winter months) - where chemical equilibration and mineral dissolution result in the
466 highest TDS concentrations across our study site (e.g., Gokhman et al., 1987; Hodgkins
467 et al., 2004; Stachnik et al., 2016; Yde et al., 2012). Layers of similar colours and
468 geochemical signatures are also found within the naled cores such as I2, I8 and I10,
469 suggestive of an eruptive process injecting these TDS-rich yellow coloured waters into
470 the ice structure. Our geophysical analysis of the substrate supports these ideas, as low
471 resistivity TMS suggests a saturated sediment layer could be fed by subglacial meltwaters

472 and/or groundwater. The geophysical survey also identifies a potential conduit for water
473 flow (~ 5 m in diameter), which could efficiently transport subsurface waters over
474 wintertime, contributing to naled ice structures when air temperatures limit overland flow.
475 The clear naled ice with low solute concentrations suggests waters have had
476 limited mineral surface contact for reactions to occur (such as supra- or englacial
477 melt/storage and/or overwinter precipitation). An alternative explanation is that these
478 layers (most often found at the top of the naled cores) are partially frozen (or partially
479 wasted) ice/slush, which just retains some of the solutes available - as the rest of the
480 solutes have either run off completely (if unconfined), or moved downwards, where they
481 have become concentrated in the bottom layer of the freezing package. For example, in
482 I8 we see very low TDS values (0.8-1.2 mg L^{-1}) in the middle of the core, followed by
483 giher concentrations of 15-141 mg L^{-1} further down the core, within the most isotopically
484 enriched layers.
485 The downcore chemical and isotopic variation in naled ice can be explained, at
486 least in part, by freezing processes. During freezing, isotopically enriched water freezes
487 first, with a stronger effect on ^{2}H than ^{18}O. Remaining, freezing water will fractionate on
488 a freezing slope unlike that of meteoric water, controlled by the initial composition of the
489 water and the fractionation factors of freezing (Jouzel and Souchez, 1982; Souchez and
490 Jouzel, 1984). In a package of ice that froze in a single outburst event, we expect the
491 heaviest isotopes on the top and lighter isotopes downcore. We also expect the
492 concentration of dissolved solutes to significantly increase at the bottom of a freezing
493 package, from the effects of progressive freeze concentration of dissolved solutes in the
494 source water (Halde, 1980).

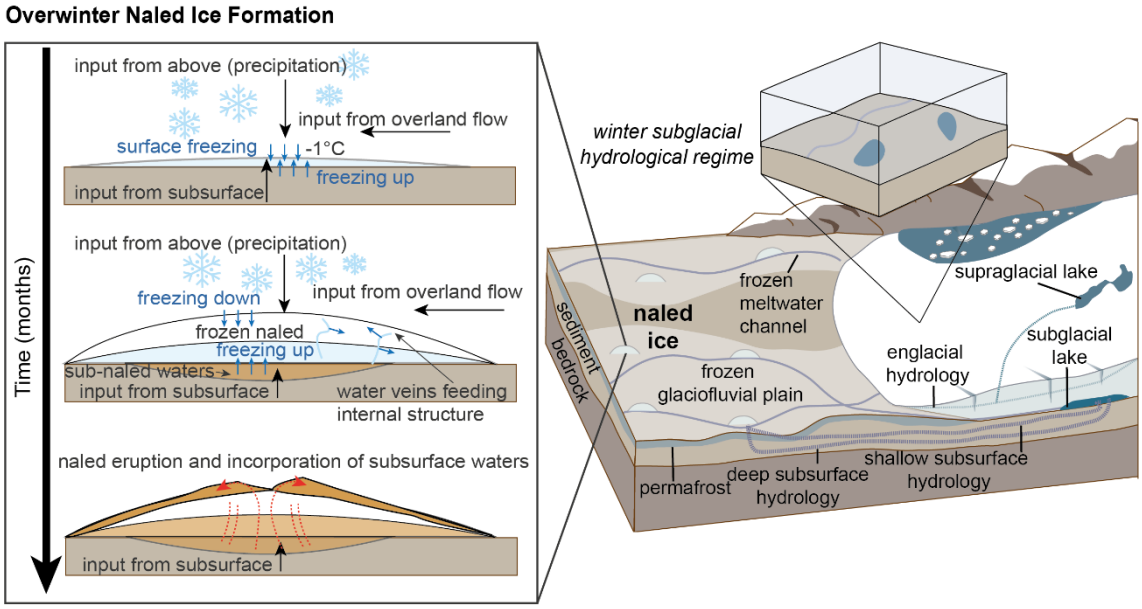


Figure 13. Conceptual diagram of naled ice formation mechanisms in western Greenland, based on ice facies, geochemical evidence and geophysical surveys of the proglacial area in front of Isunnguata Sermia. Inset box shows the evolution of naledi through winter, where water with long subsurface residence times discharges into the proglacial forefield. Other water sources, such as supraglacial and englacial melt, also contribute to naled ice layers. Naledi in this area form from both bottom-up and top-down mechanisms – incorporating two existing theories of naled formation. Water upwellings freeze onto the underside of the naled ice, and overland flow from supraglacial melt, englacial melt and precipitation freeze on top of the ice.

The stable water isotopes reveal sequential freezing downcore with discrete freezing packages resulting from multiple upwelling events. These upwellings freeze on at the base of existing ice, pushing up into the ice, and creating domed structures over wintertime. However, we also observe that in the top sections of some samples of longer cores (I2 and I7) and the shorter cores below 50 cm (I3, I4, I6 and I9) do not plot on this freezing curve. This indicates a different freezing sequence, potentially forming from a top-down process.

As water discharge is reduced over the winter months, and less glacial sediment is transported, the resulting naled ice is less sediment-laden than summer accreted ice, which forms under faster water flow conditions (Fig. 13). We therefore conclude that the naledi on the forefield of Isunnguata Sermia form through a combination of unconfined

517 and confined water sources, where subsurface waters emerge through the substrate
518 overlain by ice freeze-on below, whereas overland flows and precipitation accumulate
519 from above (Fig. 13).

520 ***5.2. Accreted ice formation mechanisms***

521 The formation of accreted ice was captured on automatic cameras in the late melt season,
522 September-October 2023, after a large upwelling event (Fig. 4; 6). Based on the speed of
523 their formation and supported by our geochemical analyses, we propose that they form
524 where supercooled meltwater is evacuated into the glacier forefield and quickly freezes
525 creating structures composed of a mix of frazil ice and silt to fine sand sediments (Fig.
526 14).

527 The accreted ice samples exhibit a moderately uniform geochemical signature
528 throughout, where the cores are dominated by sediment-rich ice layers. This uniformity
529 between sites and within each core suggests consistent water sources, potentially derived
530 from single or time-constrained outflow events. These cores are also geochemically
531 similar to previously characterised summer outflow waters in other studies (i.e., Graly et
532 al., 2014; Graly et al., 2017a). Preserved by cold air temperatures, the ice accretions
533 formed by the late melt season persist through the winter months, although gradual
534 wastage is evidenced by deflation and erosion of the ice surface towards the end of the
535 winter (due to discrete melt events), where melting leaves behind large sediment
536 accumulations. Due to our focus on overwinter ice accumulations, we were not present
537 in the summer months to observe the complete wastage of accreted ice; however, our
538 repeat field campaigns allow us to note that accreted ice structures form in almost the
539 exact same location each year. This observation indicates that the subsurface hydrological
540 system must be stable over interannual timescales.

The subglacial hydrological system in this region drives fast-moving, highly pressurised subglacial waters into the proglacial field, generating large upwellings several metres in height during summer months (Graly et al., 2017a). This water is presumably routed through the deep subglacial trough beneath Isunnguata Sermia (Lindbäck et al., 2015), where water will accumulate and interact with sediments and bedrock, before being driven up the reverse bed slope by high water pressure (when the subglacial hydrological system reaches capacity) (Cook et al., 2006; Lindbäck et al., 2014). The subsurface here is likely to be very high-porosity sand/gravel deposited during the Holocene ice margin retreat, which favours 'groundwater' flow and not channelised flow. These highly pressurised supercooled waters then freeze into large icing structures close to minimal meltwater output zones at the glacier terminus (Fig. 6, 14). Currently, the growth and wastage rates of this accreted ice formation are unknown, though we observed that sporadic hours- to days-long upwelling events contribute to the majority of the ice formation (Fig. 6a-c). We hypothesise, based on the results presented here that the formation timescale is likely fast with sudden upwellings of high velocity, highly pressurised waters erupt into the glacial forefield (Fig. 14). Where these structures are formed from single outburst events in the late summer season, they may also incorporate waters from sub-, supra- and ice-marginal lakes where their outbursts are the primary source of the upwelling (e.g., Livingstone et al., 2026).

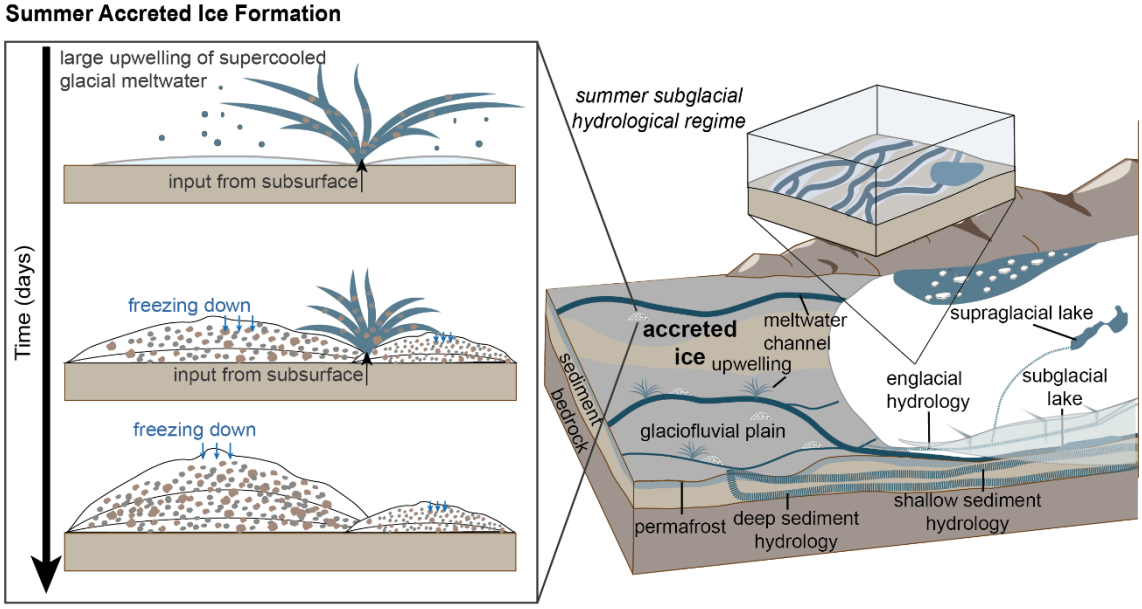


Figure 14 Conceptual diagram of accreted ice formation mechanisms in front of Isunnguata Sermia, Greenland, based on ice facies, geochemical evidence and geophysical surveys of the glacier foreland. Over summer, an efficient subglacial hydrological system moves sediment-loaded waters with low ion concentrations through subsurface hydrological pathways. This allows accreted ice to form where upwellings of highly pressurised supercooled waters erupt into the forefield and freeze adjacent to the upwelling in an isolated event.

5.3. Implications and comparisons with existing formation theories

Previous theories of naled formation have adapted either a top-down or bottom-up approach (Fig. 1). One approach details growth from waters below icing structures, with liquid water conduits within naled ice providing transport pathways insulated from the cold surface (Fig. 1f) (Stachnik et al., 2016; Wadham et al., 2000). The other approach describes accumulations from above where the cold, winter air temperature acts as a heat sink, freezing any waters or precipitation that accumulate from above (Fig. 1a-c) (Schohl and Ettema, 1986; Yde et al., 2012). Our observations and results support both of these existing theories. Winter-forming naledi at Isunnguata Sermia form through a combination of top-down and bottom-up freezing processes, whilst summer accreted ice structures form by freeze-on of higher velocity, supercooled waters erupting onto the glacier foreland.

These systems offer insights into hydrological systems in Greenland that are difficult to observe by other means. They also show how water routing can vary spatially and temporally through the melt season. Geochemical differences in ice samples also raise important questions for solute and nutrient release from the Greenland Ice Sheet. With pronounced peaks in TDS detected in the overwinter naled waters, year-round analyses of glacial waters are critical for capturing the full extent of foreland water flow and the impact of these waters on downstream ecosystems, particularly at the release of these solute-rich waters during the initial onset of the melt season. The seasonal changes in geochemistry we observe suggest that solute export in winter may be under-represented in existing literature, which should be considered for a thorough understanding of biogeochemical processes and wider ecosystem effects downstream (Hawkings et al., 2026).

6. Conclusions

Over the course of four field seasons, we have investigated the formation and build-up of winter-forming naledi and summer-forming accreted ice together for the first time, at Isunnguata Sermia, western Greenland. Using 15 ice cores, we geochemically characterised these ice structures for major ion and trace element concentrations, as well as $\delta^{2}H$ and $\delta^{18}O$ isotopic composition. By combining geochemistry with geophysical surveys and automatic camera footage, we can fully characterise and interpret icings and the hydrological pathways that drive their formation at Isunnguata Sermia for the first time. The different geochemical signatures and the stratification of ice layers in the naled cores we extracted and analysed suggest that there are multiple water sources and pathways which contribute to naled formation at Isunnguata Sermia. We detected several distinct water types within the naledi, from highly concentrated naled bottom waters enriched in dissolved ions (originating from deep hydrological sources and/or

groundwater), through to extremely dilute naled ice layers that most likely originate from supraglacial or englacial waters (which have had limited time and/or opportunity for sediment-water interaction). Our findings demonstrate how naledi can form through a combination of top-down and bottom-up freeze-on processes, where water is supplied from a variety of water sources. We suspect that similar mechanisms will create naledi elsewhere, though one process may dominate over another depending on local conditions (e.g. ice/bed topography, meltwater availability, ground conditions). In contrast, the summer accreted ice is much less geographically diverse, implying supercooled waters from the same (or similar) sources freeze-on quickly, presumably during more discrete, high-output events. By analysing icings year-round, we record a clear hydrological transition at Isunnguata Sermia, between summer (where supercooled waters emerge from efficient channelised drainage systems at pressure) and winter (where more inefficient distributed drainage networks dominate). These seasonal changes drive different geochemical outputs from the Greenland Ice Sheet. Our observations demonstrate the importance of seasonality in solute availability and show the importance of measuring glacier meltwater contributions to proglacial groundwater systems and downstream ecosystems over longer study intervals.

Data Availability

Supplementary information including all geochemical and isotope data and automatic camera GIFs are available at Zenodo doi: 10.5281/zenodo.23159526 as supplementary material. Photographs of individual ice cores and detailed methodologies are provided alongside this manuscript.

Author Contributions

Conceptualisation – JG, KW, WPG, TLH, KL

Data Curation – RM, JG, CLH, KW, WPG, TLH, MJ, JRH, FN, AMR, MT, TMT, KWo, BK, SM, HB, TK, AM, KL

Formal Analysis – RM, JG, KW, FN, MT, TMT, BK, SM, HB

Funding Acquisition – JG, KW, WPG, TLH, KL

Investigation – RM, JG, CLH, KW, WPG, TLH, MJ, JRH, FN, AMR, MT, TMT, KW, BK, SM, HB, TK, AM, KL

Methodology – RM, JG, KW, FN, MT, TMT, BK, SM, HB

Visualisation – RM, JG, KW, FN, MT, BK

Writing Original Draft – RM, JG, KW, FN

Writing Review and Editing – RM, JG, CLH, KW, WPG, TLH, MJ, JRH, FN, AMR, MT, TMT, KW, BK, SM, HB, TK, AM, KL

Competing Interests

The authors declare that they have no conflict of interest.

Acknowledgements

This work was funded by NSF-NERC grant OPP-2039854 and NE/W004860/1. The authors would like to acknowledge the support of Kangerlussuaq International Science Support (KISS) and Peter Braddock for field safety support. Geospatial support for this work provided by the Polar Geospatial Center under NSF-OPP grant OPP-2039854. The authors would also like to acknowledge Northumbria University's parental leave scheme, which provided research funding cover for KW.

References

Alley, R. B., Lawson, D. E., Evenson, E. B., Strasser, J. C., and Larson, G. J.: Glaciohydraulic supercooling: a freeze-on mechanism to create stratified, debris-rich

652 basal ice: II. Theory, Journal of Glaciology, 44, 563-569, 10.3189/S0022143000002070,
653 1998.
654 Bartholomew, I., Nienow, P., Sole, A., Mair, D., Cowton, T., Palmer, S., and Wadham,
655 J.: Supraglacial forcing of subglacial drainage in the ablation zone of the Greenland ice
656 sheet, Geophysical Research Letters, 38, 8, 10.1029/2011GL047063, 2011a.
657 Bhatia, M. P., Das, S. B., Xu, L., Charette, M. A., Wadham, J. L., and Kujawinski, E. B.:
658 Organic carbon export from the Greenland ice sheet, Geochimica et Cosmochimica Acta,
659 109, 329-344, 10.1016/j.gca.2013.02.006, 2013.
660 Blanchy, G., Saneiyan, S., Boyd, J., McLachlan, P., and Binley, A.: ResIPy, an intuitive
661 open source software for complex geoelectrical inversion/modeling, Computers &
662 Geosciences, 137, 104423, 10.1016/j.cageo.2020.104423, 2020.
663 Carey, K. L.: Icings developed from surface water and ground water, 1973.
664 Chandler, D. M., Wadham, J. L., Lis, G. P., Cowton, T., Sole, A., Bartholomew, I.,
665 Telling, J., Nienow, P., Bagshaw, E. B., Mair, D., Vinen, S., and Hubbard, A.: Evolution
666 of the subglacial drainage system beneath the Greenland Ice Sheet revealed by tracers,
667 Nature Geoscience, 6, 195-198, 10.1038/NGEO1737, 2013.
668 Chu, W., Schroeder, D. M., Seroussi, H., Creyts, T. T., Palmer, S. J., and Bell, R. E.:
669 Extensive winter subglacial water storage beneath the Greenland Ice Sheet, Geophysical
670 Research Letters, 43, 12-484, 10.1002/2016GL071538, 2016.
671 Cook, S. J., Waller, R. I., Knight, P. G., and Simon J. Cook, R. I. W., Peter G. Knight:
672 Glaciohydraulic supercooling: the process and its significance, Progress in Physical
673 Geography, 30, 577-588, 10.1177/0309133306071141, 2006.
674 Evenson, E. B., Lawson, D. E., Strasser, J. C., Larson, G. J., Alley, R. B., Ensminger, S.
675 L., and Stevenson, W. E.: Field evidence for the recognition of glaciohydrologic
676 supercooling, Glacial Processes Past and Present, 10.1130/0-8137-2337-X.23, 1999.

677 Gokhman, V. V., Gokhman, V. V., and Gokhman, V. V.: Distribution and conditions of
678 formation of glacial icings on Spitsbergen, Polar Geography, 249-260,
679 10.1080/10889378709377334, 1987.
680 Graly, J., Harrington, J., and Humphrey, N.: Combined diurnal variations of discharge
681 and hydrochemistry of the Isunnguata Sermia outlet, Greenland Ice Sheet, The
682 Cryosphere, 11, 1131-1140, 10.5194/tc-11-1131-2017, 2017a.
683 Graly, J. A., Drever, J. I., and Humphrey, N. F.: Calculating the balance between
684 atmospheric CO2 drawdown and organic carbon oxidation in subglacial hydrochemical
685 systems, Global Biogeochemical Cycles, 31, 709-727, 10.1002/2016GB005425, 2017b.
686 Graly, J. A., Humphrey, N. F., and Harper, J. T.: Chemical depletion of sediment under
687 the Greenland Ice Sheet, Earth Surface Processes and Landforms, 41, 1922-1936,
688 10.1002/esp.3960, 2016.
689 Graly, J. A., Humphrey, N. F., and Licht, K. J.: Two Metrics Describing the Causes of
690 Seasonal and Spatial Changes in Subglacial Aqueous Chemistry, Frontiers in Earth
691 Science, 6, 195, 10.3389/feart.2018.00195, 2018.
692 Halde, R.: Concentration of impurities by progressive freezing, Water Research 14, 575-
693 580, 10.1016/0043-1354(80)90115-3, 1980
694 Harden, D., Barnes, P., and Reimnitz, E.: Distribution and Character of Naleds in
695 Northeastern Alaska, Arctic, 30, 28-40, 1977.
696 Hauck, C. and Kneisel, C.: *Applied geophysics in periglacial environments* (Vol. 10).
697 Cambridge University Press, 2008.
698 Hawkings, J.R., Bradley, J.A., Doting, E.L., Hassan, N., Hendry, K.R., Holt, A.D., Hood,
699 E., Spencer, R.G., Stibal, M., Tranter, M. and Venturelli, R.A.: Glacier biogeochemical
700 cycling and downstream impacts. *Nature Reviews Earth & Environment*, 1-20,
701 10.1038/s43017-025-00751-1, 2026.

Hawkings, J., Wadham, J., Tranter, M., Telling, J., Bagshaw, E., Beaton, A., Simmons, S.-L., Chandler, D., Tedstone, A., and Nienow, P.: The Greenland Ice Sheet as a hot spot of phosphorus weathering and export in the Arctic, Global Biogeochemical Cycles, 30, 191-210, 191-210, 10.1002/2015GB005237, 2016.

Hodgkins, R., Tranter, M., and Dowdeswell, J. A.: The Characteristics and Formation of a High-Arctic Proglacial Icing, Geografiska Annaler Series A-physical Geography, 86(3), 265-275, 10.1111/j.0435-3676.2004.00230.x, 2004.

Jouzel, J. and Souchez, R. A.: Melting–Refreezing at the Glacier Sole and the Isotopic Composition of the Ice, Journal of Glaciology, 28, 35-42, 10.3189/S0022143000011771, 1982.

Kane, D. L.: Physical mechanics of aufeis growth, Canadian Journal of Civil Engineering, 8, 186-195, 1981.

Kneisel, C., Emmert, A. and Kästl, J.: Application of 3D electrical resistivity imaging for mapping frozen ground conditions exemplified by three case studies. *Geomorphology*, *210*, 71-82, 10.1016/j.geomorph.2013.12.022, 2014

Krawczyk, W.E., Lefauconnier, B. and Pettersson, L.E.: Chemical denudation rates in the Bayelva catchment, Svalbard, in the fall of 2000. *Physics and Chemistry of the Earth, Parts A/B/C*, *28*(28-32), 1257-1271, 10.1016/j.pce.2003.08.054, 2003.

Lawson, D. E., Strasser, J. C., Evenson, E. B., Alley, R. B., Larson, G. J., and Arcone, S. A.: Glaciohydraulic supercooling: a freeze-on mechanism to create stratified, debris-rich basal ice: I. Field evidence, Journal of Glaciology, 44, 547-562, 10.3189/S0022143000002069, 1998.

Lawson, E. C., Wadham, J. L., Tranter, M., Stibal, M., Lis, G. P., Butler, C. E. H., Laybourn-Parry, J., Nienow, P., Chandler, D., and Dewsbury, P.: Greenland Ice Sheet

726 exports labile organic carbon to the Arctic oceans, Biogeosciences, 11, 4015-4028,
727 10.5194/bg-11-4015-2014, 2014.
728 Lindbäck, K., Pettersson, R., Hubbard, A. L., Doyle, S. H., As, D., Mikkelsen, A. B., and
729 Fitzpatrick, A. A.: Subglacial water drainage, storage, and piracy beneath the Greenland
730 ice sheet, Geophysical Research Letters, 42, 7606-7614, 10.1002/2015GL065393, 2015.
731 Lindbäck, K., Pettersson, R., Doyle, S. H., Helanow, C., Jansson, P., Kristensen, S. S.,
732 Stenseng, L., Forsberg, R., and Hubbard, A. L.: High-resolution ice thickness and bed
733 topography of a land-terminating section of the Greenland Ice Sheet, Earth System
734 Science Data, 6, 331-338, 10.5194/essd-6-331-2014, 2014.
735 Livingstone S., Storrar R., Doyle S., Thorpe S., Moffatt A., Sole A., Chudley T. R.,
736 Gimbert F., Graly J., Licht K., Winter K., Jayarapu, A., Bagshaw, E., Barruol, G., Bauer,
737 K., Bianchi, G., Buzzard, S., Clason, C., Craw, L., Davison, B., Edwards, L., Gilhooly,
738 W., Hamilton, T. L., Hansen, C., Hawkins, J., Ing, R., Jatta, M., Jones, A., Kennedy, T.,
739 Killingbeck, S., Le Bris, T., McCerery, R., Messerli, A., Michel, A., Napoleoni, F.,
740 Peacey, M., Prior-Jones, M. R., Ross, N., Veness, R., Hepburn, A., Booth, A. Ice
741 dynamic and hydrological response to ice-dammed lake drainages at Isunnguata Sermia,
742 West Greenland, Journal of Glaciology, 2026.
743 Livingstone, S. J., Sole, A. J., Storrar, R. D., Harrison, D., Ross, N., and Bowling, J.:
744 Brief communication: Subglacial Lake drainage beneath Isunguata Sermia, West
745 Greenland: geomorphic and ice dynamic effects, The Cryosphere, 13, 2789-2796,
746 10.5194/tc-13-2789-2019, 2019.
747 Mallinson, L., Swift, D. A., and Sole, A. J.: Proglacial icings as indicators of glacier
748 thermal regime: ice thickness changes and icing occurrence in Svalbard, Geografiska
749 Annaler Series A-physical Geography, 101(4), 334-349,
750 10.1080/04353676.2019.1670952, 2019.

751 Meierbachtol, T., Harper, J., and Humphrey, N.: Basal drainage system response to
752 increasing surface melt on the Greenland Ice Sheet, Science, 341, 777-779,
753 10.1126/science.1235905, 2013.
754 Meire, L., Meire, P., Struyf, E., Krawczyk, D. W., Arendt, K. E., Yde, J. C., Pedersen, T.
755 J., Hopwood, M. J., Rysgaard, S., and Meysman, F. J. R.: High export of dissolved silica
756 from the Greenland Ice Sheet, Geophysical Research Letters, 43, 9173-9182,
757 10.1002/2016GL070191, 2016.
758 Morse, P. D. and Wolfe, S. A.: Geological and meteorological controls on icing (aufeis)
759 dynamics (1985 to 2014) in subarctic Canada, Journal of Geophysical Research: Earth
760 Surface, 120, 1670-1686, 10.1002/2015JF003534, 2015.
761 Pain, A. J., Martin, J. B., Martin, E. E., Rennermalm, Å. K., and Rahman, S.:
762 Heterogeneous CO2 and CH4 content of glacial meltwater from the Greenland Ice Sheet
763 and implications for subglacial carbon processes, The Cryosphere, 15, 1-33, 10.5194/tc-
764 15-1627-2021, 2021.
765 Palacky, G.J.: Resistivity characteristics of geologic targets, In: Electromagnetic methods
766 in applied geophysics, 10.1190/1.9781560802631.ch3, 1987
767 Pitcher, L. H., Smith, L. C., Gleason, C. J., Miège, C., Ryan, J. C., Hagedorn, B., van As,
768 D., Chu, W., and Forster, R. R.: Direct observation of winter meltwater drainage from the
769 Greenland Ice Sheet, Geophysical Research Letters, 47, e2019GL086521,
770 10.1029/2019GL086521, 2020.
771 Porter, C., Howat, I., Noh, M.J., Husby, E., Khuvis, S., Danish, E., Tomko, K., Gardiner,
772 J., Negrete, A., Yadav, B., Klassen, J., Kelleher, C., Cloutier, M., Bakker, J., Enos, J.,
773 Arnold, G., Bauer, G., and Morin, P., 2023, "ArcticDEM – Mosaics, Version 4.1",
774 https://doi.org/10.7910/DVN/3VDC4W, Harvard Dataverse, V1, [01/09/2024].

775 Reynolds, J.M.: An introduction to applied and environmental geophysics. John Wiley &
776 Sons., 2011
777 Roberts, M. J., Russell, A. J., Tweed, F. S., and Knudsen, Ó.: Controls on englacial
778 sediment deposition during the November 1996 jökulhlaup, Skeiðarárjökull, Iceland,
779 Earth Surface Processes and Landforms, 26, 935-952, 10.1002/esp.236, 2001.
780 Roberts, M. J., Tweed, F. S., Russell, A. J., Knudsen, O. S., Lawson, D. E., Larson, G. J.,
781 Evenson, E. B., and Björnsson, H.: Glaciohydraulic supercooling in Iceland, Geology,
782 30, 871-874, 10.1130/0091-7613(2002)030, 2002.
783 Schohl, G. A. and Ettema, R.: Theory and Laboratory Observations of Naled Ice Growth,
784 Journal of Glaciology, 32, 168-177, 10.3189/S0022143000015483, 1986.
785 Sobota, I.: Icings and their role as an important element of the cryosphere in High Arctic
786 glacier forefields, Bulletin of Geography: Physical Geography Series, 81-93,
787 10.1515/bgeo-2016-0006, 2016.
788 Sodemann, H., Mørkved, P. T., and Wahl, S.: FLIIMP - a community software for the
789 processing, calibration, and reporting of liquid water isotope measurements on cavity-
790 ring down spectrometers, MethodsX, 11, 102297, 10.1016/j.mex.2023.102297, 2023.
791 Souchez, R. A. and Jouzel, J.: On the Isotopic Composition in δD and δ18O of Water and
792 Ice During Freezing, Journal of Glaciology, 30, 369-372, 10.3189/S0022143000006249,
793 1984.
794 Stachnik, L., Yde, J. C., Kondracka, M., D., I., and Grzesik, M.: Glacier naled evolution
795 and relation to the subglacial drainage system based on water chemistry and GPR surveys
796 (Werenskioldbreen, SW Svalbard), Annals of Glaciology, 57, 19-30,
797 10.1017/aog.2016.9, 2016.
798 van Gool, J. A. M., Connelly, J. N., Marker, M., and Mengel, F. C.: The Nagssugtoqidian
799 Orogen of West Greenland: Tectonic evolution and regional correlations from a West

800 Greenland perspective, Canadian Journal of Earth Science, 39, 665-686, 10.1139/E02-
801 027, 2002.
802 Wadham, J. L., Tranter, M., and Dowdeswell, J. A.: Hydrochemistry of meltwaters
803 draining a polythermal-based, high-Arctic glacier, south Svalbard: II. Winter and early
804 Spring, Hydrological Processes, 14, 1767-1786, 10.1002/1099-
805 1085(200007)14:10<1767:aid-hyp103>3.0.co;2-q, 2000.
806 Wadham, J. L., Hawkings, J., Telling, J., Chandler, D., Alcock, J., O'Donnell, E., Kaur,
807 P., Bagshaw, E., Tranter, M., Tedstone, A., and Nienow, P.: Sources, cycling and export
808 of nitrogen on the Greenland Ice Sheet, Biogeosciences, 13, 6339-6352, 10.5194/bg-13-
809 6339-2016, 2016.
810 Weng, Y., Touzeau, A. and Sodemann, H.: Correcting the impact of the isotope
811 composition on the mixing ratio dependency of water vapour isotope measurements with
812 cavity ring-down spectrometers, Atmospheric Measurement Techniques, 13(6), 3167-
813 3190, 2020.
814 Yde, J. C., Knudsen, N. T., Hasholt, B., and Mikkelsen, A. B.: Meltwater chemistry and
815 solute export from a Greenland Ice Sheet catchment, Watson River, West Greenland,
816 Journal of Hydrology, 519, 2165-2179, 10.1016/j.jhydrol.2014.10.018, 2014.
817 Yde, J. C., Hodson, A. J., Solovjanova, I., Steffensen, J. P., Nørnberg, P., Heinemeier, J.,
818 and Olsen, J.: Chemical and isotopic characteristics of a glacier-derived naled in front of
819 Austre Grønfjordbreen, Svalbard, Polar Research, 31, 17628, 10.3402/polar.v31i0.17628,
820 2012.
821 Yoshikawa, K., Hinzman, L. D., and Kane, D. L.: Spring and aufeis (icing) hydrology in
822 Brooks Range, Alaska, Journal of Geophysical Research: Biogeosciences, 112(G4),
823 10.1029/2006JG000294, 2007.